ACS NANO

www.acsnano.org

ARTICLE

Accelerating Palladium Nanowire H_2 Sensors Using Engineered Nanofiltration

Won-Tae Koo,[†] Shaopeng Qiao,[‡] Alana F. Ogata,[§] Gaurav Jha,[§] Ji-Soo Jang,[†] Vivian T. Chen,[§] Il-Doo Kim,*[,†] and Reginald M. Penner*[,§]

[†]Department of Materials Science and Engineering, Korea Advanced Institute of Science and Technology (KAIST), 291 Daehak-ro, Yuseong-gu, Daejeon 34141, Republic of Korea

[‡]Department of Physics and [§]Department of Chemistry, University of California, Irvine, California 92697-2025, United States

Supporting Information

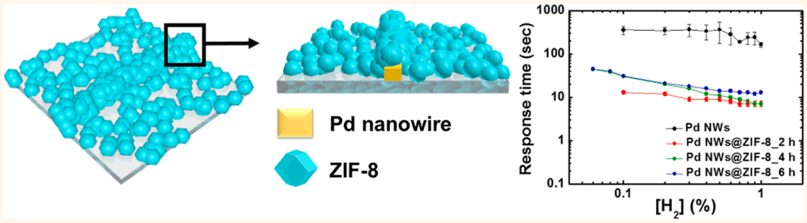

ABSTRACT: **The oxygen, O_2, in air interferes with the detection of H_2 by palladium (Pd)-based H_2 sensors, including Pd nanowires (NWs), depressing the sensitivity and retarding the response/recovery speed in air—relative to N_2 or Ar. Here, we describe the preparation of H_2 sensors in which a nanofiltration layer consisting of a Zn metal−organic framework (MOF) is assembled onto Pd NWs. Polyhedron particles of Zn-based zeolite imidazole framework (ZIF-8) were synthesized on lithographically patterned Pd NWs, leading to the creation of ZIF-8/Pd NW bilayered H_2 sensors. The ZIF-8 filter has many micropores (0.34 nm for gas diffusion) which allows for the predominant penetration of hydrogen molecules with a kinetic diameter of 0.289 nm, whereas relatively larger gas molecules including oxygen (0.345 nm) and nitrogen (0.364 nm) in air are effectively screened, resulting in superior hydrogen sensing properties. Very importantly, the Pd NWs filtered by ZIF-8 membrane (Pd NWs@ZIF-8) reduced the H_2 response amplitude slightly ($\Delta R/R_0$ = 3.5% to 1% of H_2 *versus* 5.9% for Pd NWs) and showed 20-fold faster recovery (7 s to 1% of H_2) and response (10 s to 1% of H_2) speed compared to that of pristine Pd NWs (164 s for response and 229 s for recovery to 1% of H_2). These outstanding results, which are mainly attributed to the molecular sieving and acceleration effect of ZIF-8 covered on Pd NWs, rank highest in H_2 sensing speed among room-temperature Pd-based H_2 sensors.**

KEYWORDS: *metal−organic framework, electrodeposition, Pd nanowire, response, recovery, hydrogen gas sensor*

Hydrogen (H_2) has been regarded as a next-generation energy source due to its abundance in nature and high efficiency in energy combustion.[1] In particular, the combustion reaction of hydrogen produces only water (H_2O) as a byproduct, thus H_2-based energy systems have attracted attention as clean energy sources. However, the application of H_2 as a fuel is complicated by its flammability: the lower explosion limit for H_2 in air of 4%. When coupled with the fact that H_2 is odorless, this imposes the requirement that sensors should be used to detect leaked H_2 wherever it is in use.[2] Safety is the driver for the development of high-performance hydrogen gas sensors that respond and recover rapidly, are inexpensive, and are capable of detecting H_2 well below 4%. With the development of a next-generation sensing platform, such as the Internet of things system, the gas sensors can be applied in major parts of human life. Thus, real-time detection of H_2 leakage can be realized by developing ultrafast H_2 gas sensors.[3,4]

Among the various types of hydrogen gas sensors, palladium (Pd)-based resistor-type hydrogen sensors have been widely studied because of their simplicity, low cost, and adequate sensitivity, but the response and recovery speed of these H_2 sensors—even those based upon nanoscopic Pd sensing elements—has been insufficient.[5] In general, there are two types of Pd-based H_2 sensors. Because the reaction of Pd with H_2 induces the increase of the Pd base resistance by forming PdH_x, H_2 can be easily detected by monitoring the resistance variation of Pd, even at room temperature (RT). On the other hand, H_2 in the range from 1−2% can be detected by utilizing the volume expansion of β phase PdH_x. Since the phase transition of α-Pd to β-PdH_x causes volume expansion, the break junctions in Pd can be connected, leading to a decrease of

Received: June 28, 2017
Accepted: August 18, 2017
Published: August 18, 2017

DOI: 10.1021/acsnano.7b04529
ACS Nano 2017, 11, 9276−9285

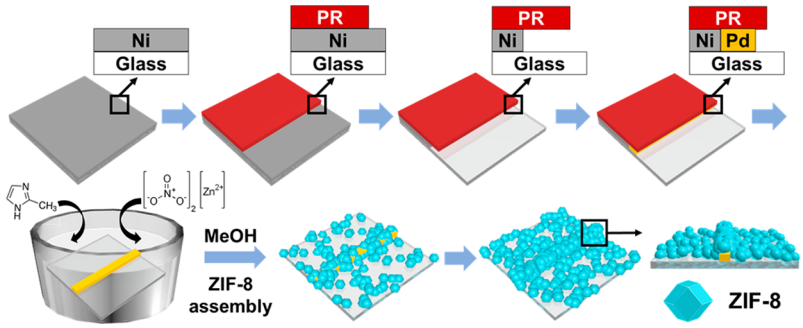

Figure 1. (a) Schematic illustration of synthesis of Pd NWs@ZIF-8 using LPNE process and following assembly process. Detail of each process is described in the Experimental Section.

the resistance of the Pd-based sensors. This type of sensor can detect hydrogen with fast response speed,[3] but the range over which H_2 can be detected is limited to the α to β phase transition of the PdH_x (over 1−2% range). So far, a number of Pd-based hydrogen sensors, including Pd nanowires (NWs),[6−8] Pd nanotubes,[9,10] Pd films,[11−13] and Pd NW networks,[14] have been suggested. However, these hydrogen sensing properties have been evaluated in nitrogen (N_2) atmospheres, not in air. As there are a number of gas species in air, the sensing performance of Pd can be significantly degraded by interfering gases including oxygen (O_2), sulfur dioxide (SO_2), or hydrogen sulfide (H_2S).[15] For example, in air, chemisorbed O (Pd−O) reacts with adsorbed dihydrogen on the surface of Pd to produce water.[16]

$$\mathrm{Pd-O} + \frac{3}{2}\mathrm{H_2\,(ads)} \rightarrow \mathrm{Pd-H} + \mathrm{H_2O\,(ads)} \quad (1)$$

$$\mathrm{H_2O\,(ads)} \rightarrow \mathrm{H_2O\,(gas)} \quad (2)$$

These reactions reduce the steady-state coverage of the Pd surface by chemisorbed H, resulting in a decreased rate of H absorption into the PdH_x as well as lower steady-state values of x. Moreover, oxygen species adsorbed on the Pd surface block adsorption sites for hydrogen. For these reasons, poor hydrogen sensing responses and sluggish reaction kinetics are often observed in Pd-based sensors, particularly in ambient air. To minimize the screening effect of O_2 on Pd NW-based sensor, Li *et al.*[17] proposed the functionalization of Pt catalysts on Pd NWs. Because Pt catalysts accelerate the removal of oxygen from the Pd surface as water, enhanced hydrogen detection performance was observed. However, for the activation of Pt catalysts, the sensors were operated at a high temperature (100 °C), leading to the degradation of the detection limit of these sensors.

Metal−organic frameworks (MOFs) consisting of metal nodes and organic linkers are finding application in catalysis,[18] gas separation,[19] gas sensors,[20−22] drug delivery,[23] and so on,[24,25] due to the incredibly high surface area, ultrahigh porosity, and tunability of these versatile materials.[26,27] Among the various types of MOFs, the zinc (Zn)-based zeolite imidazole framework (ZIF-8) has been widely studied due to its facile synthesis by simple precipitation reaction in solvents such as water or methanol and because of its high stability.[28,29] In particular, ZIF-8 has a high hydrogen permeability due to its microporous cavity structure characterized by 0.34 nm diameter pores that allow selective penetration of H_2 (0.289 nm) molecules, whereas virtually all other gas molecules (>0.34 nm) are excluded.[30,31] Recently, ZIF-8 was used as a protection layer for selective H_2 sensing of ZnO-based sensing materials.[32,33] In that work, Zn ions on the surface of ZnO were thought to facilitate the nucleation and growth of ZIF-8. The ZnO surrounded by the ZIF-8 membrane showed improved hydrogen sensing properties. Although semiconducting metal−oxide (SMO) sensors have been successfully commercialized, their operation temperature is relatively high (250−400 °C) and a strong humidity dependence hampers the reliability of SMO sensors, particularly when they are operated at RT.[34] To achieve the H_2 sensing performance targeted in recent guidelines issued by the U.S. Department of Energy (DOE)[35] (response time <1 s ($[H_2]$ = 4%) and <60 s ($[H_2]$ = 1%), and recovery time <60 s), H_2 sensors with faster response and recovery performance must be developed.

Here, we propose bilayered hydrogen sensors, consisting of lithographically patterned Pd NWs overcoated with a ZIF-8 molecular sieving layer (Pd NWs@ZIF-8). Patterned Pd NWs prepared by lithographically patterned NW deposition (LPNE) process represent the current state-of-the-art technology for hydrogen gas sensors.[8,17] However, the response and recovery performance of these sensors still falls short of DOE targets. To overcome the inherent limitation of Pd-based H_2 sensors, in this work, ZIF-8 was assembled on Pd NWs as a protection layer that facilitates the adsorption and desorption of H_2. The ZIF-8 nanofiltration layer is grown on arrays of Pd NWs by heterogeneous nucleation from solution-phase precursors. We found that the MOF nanofiltration layer accelerates H_2 response and recovery by a factor of 20 in air.

RESULTS AND DISCUSSION

The fabrication of Pd NWs@ZIF-8 hydrogen sensors is depicted schematically in Figure 1. Pd NWs are first prepared using the LPNE process as previously described.[17] This process involves the evaporation of 40 nm nickel films onto glass. Then, a photoresist (PR) layer is spin-coated onto the nickel-coated glass substrate. This PR layer is lithographically patterned using a contact mask and ultraviolet exposure, and after development, the exposed Ni was etched with nitric acid—a process that also produces a horizontal trench at the edge of the PR layer. Pd NWs are then electrodeposited within this trench, and the residual PR and Ni are removed by acetone and nitric acid, respectively. Finally, the ZIF-8 nanofiltration layer is prepared by immersion of the glass substrates patterned with Pd NWs into methanol (MeOH) that contain the Zn precursors ($Zn(NO_3)_2{\cdot}6H_2O$) and 2-methylimidazole (mIM). This process assembles the ZIF-8 by heterogeneous nucleation onto both the Pd NWs and the glass substrate. To investigate the deposition of ZIF-8, we controlled the assembly time to 2 h,

DOI: 10.1021/acsnano.7b04529
ACS Nano 2017, 11, 9276−9285

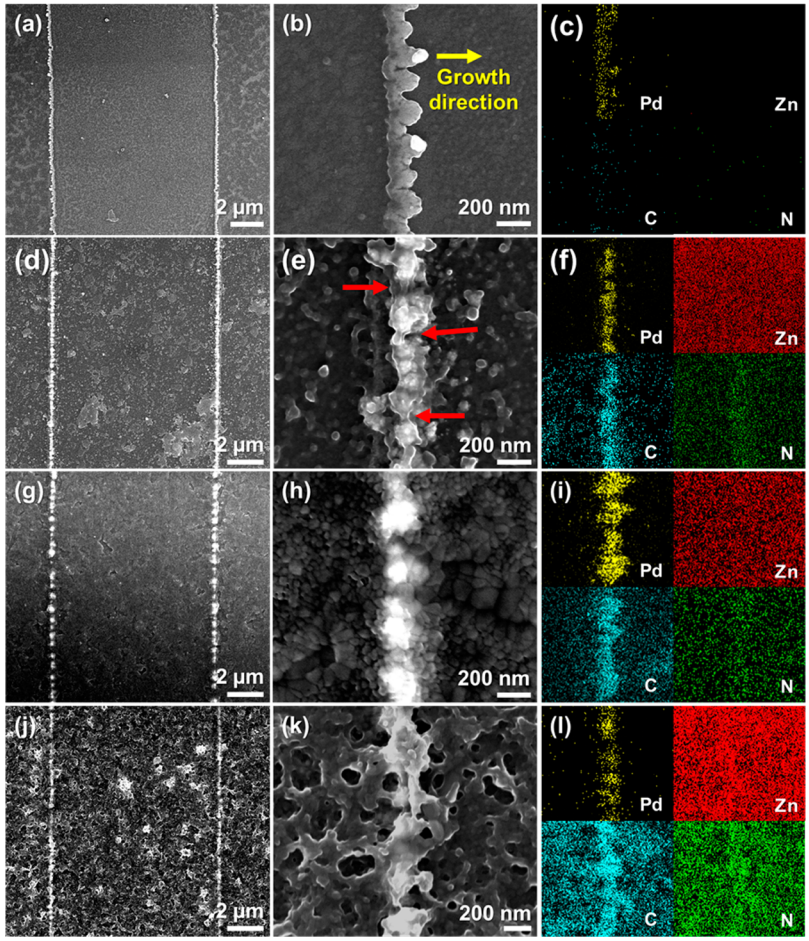

Figure 2. SEM and EDS elemental images of Pd NWs (a–c), Pd NWs@ZIF-8_2 h (d–f), Pd NWs@ZIF-8_4 h (g–i), and Pd NWs@ZIF-8_6 h (j–l) on the glass substrate. Low-magnification SEM images of the samples with patterned Pd NWs (a gap of 10 μm) (a,d,g,j), high-magnification SEM images of the samples (b,e,h,k), and EDS elemental mapping images of each sample (c,f,i,l).

4 h, and 6 h. Here after, Pd NWs@ZIF-8_2 h, 4 h, and 6 h denote Pd NWs@ZIF-8 self-assembled for durations of 2 h, 4 h, and 6 h, respectively. Then, the samples were washed with ethanol five times to remove residual precursors and ZIF-8 that is not tightly bound on the surface and finally dried for 24 h at RT to activate ZIF-8.

The morphologies of the samples were analyzed using scanning electron microscopy (SEM) (Figure 2). Figure 2a shows an array of linear Pd NWs deposited at a 10 μm pitch. The magnified image clearly revealed the rough surface of the Pd NW with an average diameter of 200 ± 50 nm (Figure 2b). In addition, the SEM image also revealed the growth direction of the Pd NW (yellow arrow in Figure 2b). The Pd element was confirmed by the energy-dispersive X-ray spectrometry (EDS) elemental mapping images using SEM (Figure 2c). After assembly in MeOH for 2 h, ZIF-8 was directly grown on the Pd NWs (Figure 2d,e). The surface of Pd NW was covered by the ZIF-8, and some ZIF-8 was also deposited on the glass substrate. In addition, there are necking points on the Pd NWs@ZIF-8_2 h (red arrows in Figure 2e), which are caused by the rugged surface of the Pd NW. In EDS mapping images of Pd NWs@ZIF-8_2 h, we observed the elements of Pd, Zn, carbon (C), and nitrogen (N) (Figure 2f). Because the glass substrate is hydrophilic, Zn ions can be easily combined with the surface of the glass. Therefore, Zn was observed on the entire substrates. On the other hand, the mapping images of C and N are predominantly concentrated on the top surface of the Pd NW. Because the organic ligands of ZIF-8 (*i.e.*, mIM) consisted of C, N, and H, this result indicates that the growth of ZIF-8 on Pd NWs is faster than that on the glass substrate. In the case of ZIF-8 assembled for 4 h, ZIF-8 was uniformly grown on both the glass substrate (Figure 2g) and Pd NWs (Figure 2h). The background intensity of C and N is increased (Figure 2i) compared to that of Pd NWs@ZIF-8_2 h in Figure 2f. For Pd NWs@ZIF-8_6 h, thick ZIF-8 film was formed (Figure 2j), and the slight agglomeration of ZIF-8 was also observed (Figure 2k). The Pd NW was entirely embedded in the ZIF-8 membrane, as shown in the EDS mapping images (Figure 2l).

To investigate the surface morphology and thickness of ZIF-8 on Pd NW patterned glass substrate, we conducted atomic force microscopy (AFM). The height of pristine Pd NWs synthesized by LPNE process is about 38 ± 2 nm (Figure S1a). As shown in Figure S1b, the height of Pd NWs@ZIF-8_2 h is increased to 160 ± 20 nm, indicating the preferential growth of ZIF-8 on Pd NWs. As the ZIF-8 growth time is increased to 4 and 6 h, thicker ZIF-8 is uniformly deposited on the surface of the Pd NW patterned glass substrate. However, as the ZIF-8 is also assembled on the glass substrate, the relative height of ZIF-8 on the Pd NW is decreased to 130 ± 15 nm for Pd NWs@ZIF-8_4 h and 35 ± 10 nm for Pd NWs@ZIF-8_6 h (Figure S1c,d). On the other hand, cross-sectional SEM images clearly show the thickness of ZIF-8 on Pd NWs. The yellow box in

DOI: 10.1021/acsnano.7b04529
ACS Nano 2017, 11, 9276–9285

each cross-section image indicates the region which is presumably the Pd NW. Figure S1e shows that ZIF-8 with a thickness of 167 nm was selectively grown on the surface of the Pd NW after the assembly for 2 h. After 4 h of assembly, the thickness of ZIF-8 is slightly increased (201 nm) (Figure S1f), and a ZIF-8 layer is also deposited on the glass substrate. On the other hand, Pd NWs@ZIF-8_6 h shows that all the Pd NWs and glass substrate are covered by the thick layer (330 nm) of ZIF-8 (Figure S1g).

The growth of ZIF-8 on the Pd NWs and the glass substrate is initiated by heterogeneous nucleation. In general, heterogeneous nucleation is more facile than homogeneous nucleation because the critical Gibbs free energy for heterogeneous nucleation is lower than that of homogeneous nucleation.[36] In addition, a site with high surface energy, such as dislocation, grain boundary, or edge site promotes higher nucleation rates compared to low-energy sites characterized by an absence of defects. In our experiments, the Pd NWs and the glass substrate acted as heterogeneous sites for ZIF-8 nucleation. The Pd NWs synthesized by LPNE process had a polycrystalline structure with a rough surface, and the glass (SiO_2) substrate exhibited a smooth surface due to its amorphous nature and chromium etching process. This means that the Pd NWs have a higher internal surface energy than the glass substrate. Therefore, the ZIF-8 layer quickly covers the surface of the Pd NWs relative to the glass substrate.

The crystal structure of Pd NWs@ZIF-8 was investigated by grazing incidence X-ray diffraction (XRD). As shown in Figure 3, the peaks related to Pd NWs were not observed in XRD

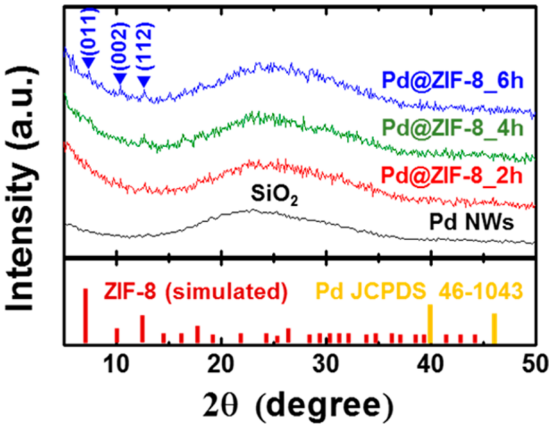

Figure 3. Grazing incidence XRD patterns of Pd NWs, Pd NWs@ZIF-8_2 h, Pd NWs@ZIF-8_4 h, and Pd NWs@ZIF-8_6 h on the glass substrate.

analysis due to the low intensity of Pd (40 nm (height) × 200 nm (width) spaced laterally by 10 μm). The background peak is associated with the glass substrate (amorphous SiO_2). On the other hand, in the case of Pd NWs@ZIF-8 samples, the weak intensities of ZIF-8 main planes of (011), (002), and (112) were observed in the XRD data (blue marks on Figure 3), which is consistent with previous studies on ZIF-8.[21,37] To further confirm the XRD peaks of ZIF-8, we prepared Pd NWs@ZIF-8 samples gently washed one time (Figure S2). Because the sample was not fully washed, there are residual Zn sources, mIM, and ZIF-8 which is not bound to the substrate. Thus, the residual Zn sources and mIM can assemble each other and produce the additional ZIF-8 layers on the glass substrate (Figure S2a,b). The EDS elemental mapping images showed the existence of Pd NWs and ZIF-8 on the substrate (Figure S2c). Although the surface of the sample is slightly agglomerated, the XRD result of the sample clearly shows the ZIF-8 peaks (Figure S2d), demonstrating the synthesis of ZIF-8 on the substrate.

In order to investigate the critical role of ZIF-8 as a molecular sieving layer on Pd NWs, we carried out hydrogen gas sensing analysis using pristine Pd NWs, Pd NWs@ZIF-8_2 h, Pd NWs@ZIF-8_4 h, and Pd NWs@ZIF-8_6 h. To verify the resistance change, we deposited a gold (Au) electrode (gap is 20 μm) between Pd NWs (Figure S3), and subsequently, ZIF-8 was assembled on the sensors. First, the sensing measurement was carried out in the hydrogen concentration range of 0.02 to 1% at RT in air. Detailed sensing measurements are described in the Experimental Section. The dynamic resistance transients of Pd NWs, Pd NWs@ZIF-8_2 h, Pd NWs@ZIF-8_4 h, and Pd NWs@ZIF-8_6 h are shown in Figure 4. The baseline resistance (500 Ω for Pd NWs, 20 kΩ for Pd NWs@ZIF-8_2 h, 155 kΩ for Pd NWs@ZIF-8_4 h, and 203 kΩ for Pd NWs@ZIF-8_6 h) of samples is increased as the thickness of ZIF-8 layers is increased, which might be caused by the increase of contact resistances. Because ZIF-8 is an insulating material with high band gap (5.5 eV),[38] the ZIF-8 deposited on Au electrodes during the sensor fabrication can increase the baseline resistances. The pristine Pd NWs exhibited hydrogen sensing response at RT in air (Figure 4a). However, the Pd NWs did not show the sensing properties below 0.1% of hydrogen (Figure 4b). The periodic decrease of the baseline resistance after hydrogen exposure is not yet known, but this phenomenon was also observed in previous literature.[15] On the other hand, the Pd NWs@ZIF-8 samples show stable resistance transients even in short-term exposure time (30 s for Pd NWs@ZIF-8_2 h and 60 s for Pd NWs@ZIF-8_4 h and Pd NWs@ZIF-8_6 h). Considering that the stable dynamic resistance transients of Pd NWs are obtained at an exposure time of 600 s, remarkably reduced response and recovery times of Pd NWs were achieved by introducing the ZIF-8 membrane. The Pd NWs@ZIF-8_2 h showed fastest response and recovery speed (Figure 4c) among the Pd NWs@ZIF-8, but the sensor did not detect the low level of hydrogen molecules (Figure 4d). However, the detection limit of Pd NWs@ZIF-8_4 h and Pd NWs@ZIF-8_6 h is down to 0.06% (600 ppm) while maintaining reasonably high response and recovery speed (Figure 4e–h). The hydrogen sensing properties at a concentration less than 0.04% of hydrogen were not accurately identified due to the resistance change from the noise.

To clearly compare sensing properties, we characterized gas response, response time, and recovery time of the four different sensors, that is, pure Pd NWs, Pd NWs@ZIF-8_2 h, Pd NWs@ZIF-8_4 h, and Pd NWs@ZIF-8_6 h (Figure 5). Response of sensors is defined as the ratio ($\Delta R_{max}/R_0$ (%)) of maximum resistance change (ΔR_{max}) to baseline resistance (R_0). Response and recovery times are the time necessary for the resistance to increase from R_0 to $R_0 + 0.9\Delta R_{max}$ and the time for the resistance to decrease from $R_0 + \Delta R_{max}$ to $R_0 + 0.1\Delta R_{max}$. The error bars in each graph represent the sensing properties of three independent hydrogen sensors for each of the four sensor archetypes. The hydrogen responses of the sensors are plotted in Figure 5a. In the range of 0.3–1% hydrogen, the Pd NWs exhibited higher response than the Pd NWs@ZIF-8. To 1% of hydrogen, the response of each sample is 5.88% for pristine Pd NWs, 1.93% for Pd NWs@ZIF-8_2 h, 3.47% for Pd NWs@ZIF-8_4 h, and 2.39% for Pd NWs@ZIF-8_6 h. However, the

DOI: 10.1021/acsnano.7b04529
ACS Nano 2017, 11, 9276–9285

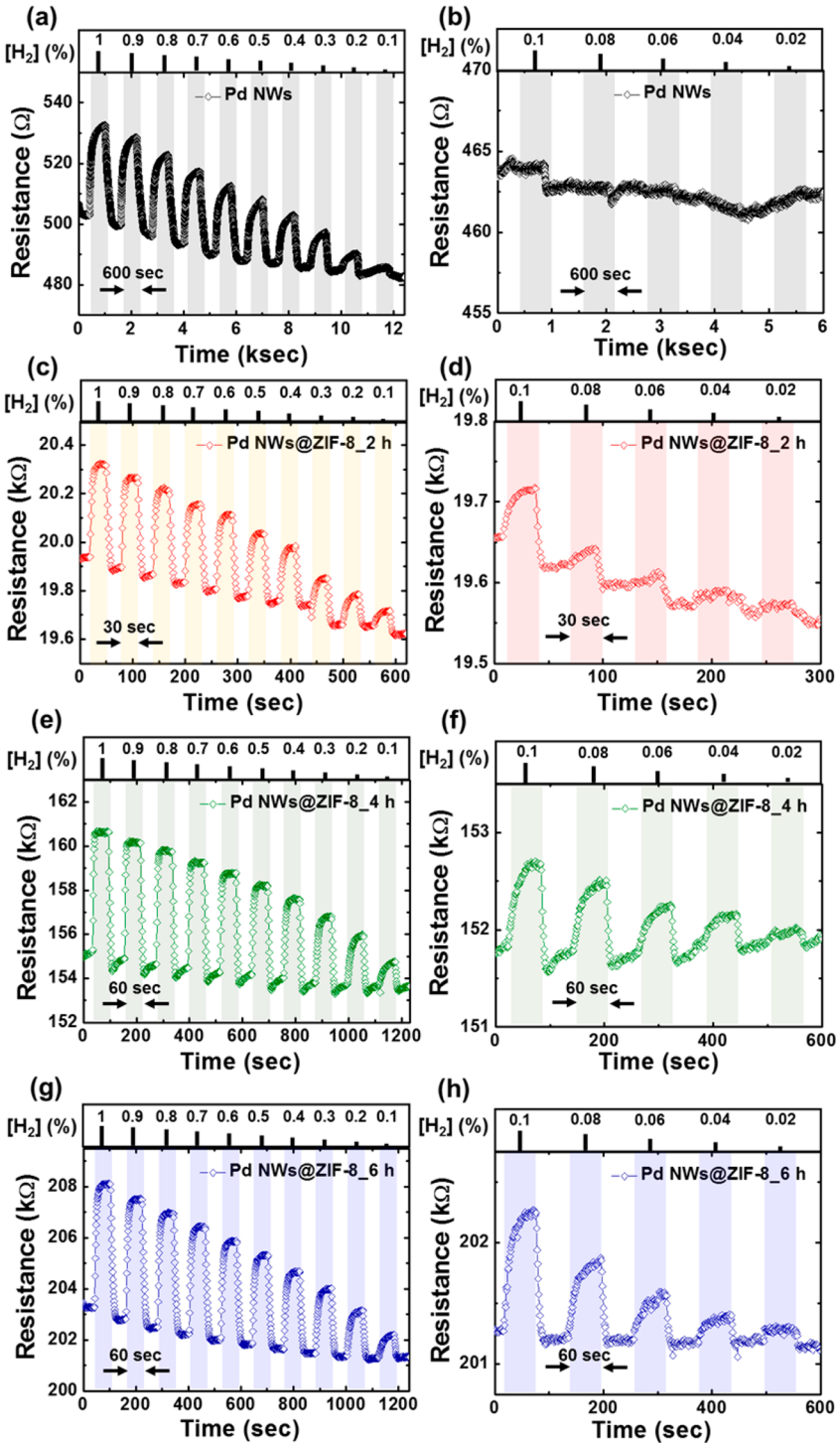

Figure 4. Dynamic baseline resistance transitions in the concentration range of 0.02−1% [H_2] at RT. (a) Pd NWs, (b) Pd NWs@ZIF-8_2 h, (c) Pd NWs@ZIF-8_4 h, and (d) Pd NWs@ZIF-8_6 h. The exposure times to hydrogen (for response) and air (for recovery) are 600 s for Pd NWs, 30 s for Pd NWs@ZIF-8_2 h, and 60 s for Pd NWs@ZIF-8_4 h and Pd NWs@ZIF-8_6 h.

response of Pd NWs is rapidly decreased in low level (0.1−0.2%) of hydrogen. The rapid decrease in response of Pd NW is explained by the oxygen effect in air. Oxygen can react with adsorbed hydrogen on the surface of Pd (eqs 1 and 2), and at low concentrations, the response may be greatly affected by the reaction. Thus, the response is drastically decreased. On the other hand, Pd NWs@ZIF-8 samples exhibited higher response (0.31% for Pd NWs@ZIF-8_2 h, 0.69% for Pd NWs@ZIF-8_4 h, and 0.46% for Pd NWs@ZIF-8_6 h) than Pd NWs (0.17%) to 0.1% of hydrogen. In addition, Pd NWs@ZIF-8_4 h shows higher response than Pd NWs@ZIF-8_2 h and Pd NWs@ZIF-8_6 h in all ranges of hydrogen.

The response and recovery times of sensors are dramatically improved by the ZIF-8 layer (Figure 5b,c). The response time to 1% of hydrogen is 7 s for Pd NWs@ZIF-8_2 h and Pd NWs@ZIF-8_4 h and 13 s for Pd NWs@ZIF-8_6 h, whereas that of Pd NWs is 164 s (Figure 6a). In addition, the recovery time toward 1% of hydrogen is 8 s for Pd NWs@ZIF-8_2 h, 10

DOI: 10.1021/acsnano.7b04529
ACS Nano 2017, 11, 9276−9285

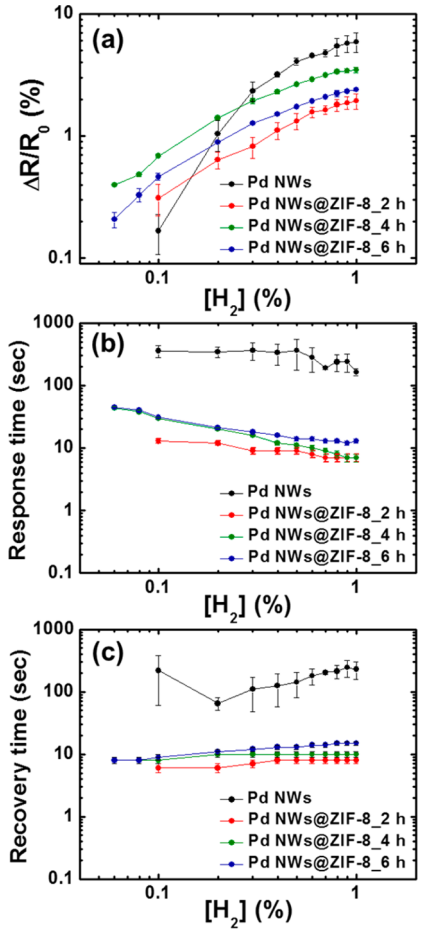

Figure 5. Hydrogen sensing metrics for Pd NWs, Pd NWs@ZIF-8_2 h, Pd NWs@ZIF-8_4 h, and Pd NWs@ZIF-8_6 h. (a) Response *versus* [H_2] in air, (b) response time *versus* [H_2] in air, and (c) recovery time *versus* [H_2].

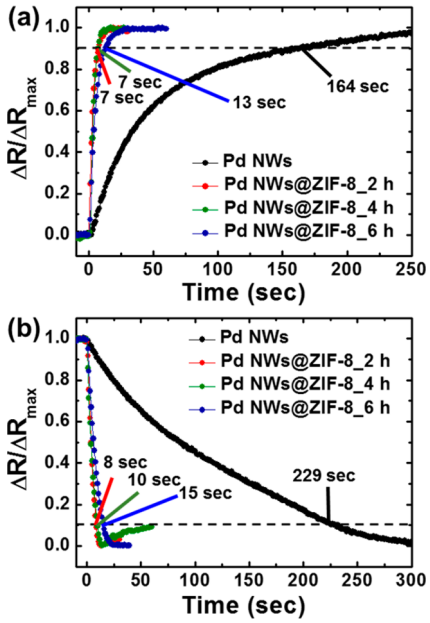

Figure 6. Normalized curves of response (a) and reocvery (b) for Pd NWs, Pd NWs@ZIF-8_2 h, Pd NWs@ZIF-8_4 h, and Pd NWs@ZIF-8_6 h. [H_2] = 1% in air. The horizontal dashed line indicates $\Delta R/R_{max}$ = 0.90 for response and $\Delta R/R_{max}$ = 0.1 for recovery.

s for Pd NWs@ZIF-8_4 h, 15 s for Pd NWs@ZIF-8_6 h, and 229 s for Pd NWs (Figure 6b). Although the response time of Pd NWs@ZIF-8 is slightly increased in the low concentration range, the response time of Pd NWs@ZIF-8 is faster than that of Pd NWs by over 10-fold (Figure 5b). In addition, the recovery time of the sensors in the low concentration range is further decreased. The sensing properties of other Pd-based materials operated at RT in air are summarized in Table 1.[6,7,9,10,13,17] Although the response of Pd NWs@ZIF-8 is lower than other Pd-based sensors in previous literature, response time and recovery time of the sensors are extremely fast. The Pd NWs@ZIF-8 represents the current state-of-the-art technology in terms of response and recovery time.

The improvement in hydrogen sensing properties of Pd NWs@ZIF-8 is described by the molecular sieving effect and acceleration effect of ZIF-8 (Figure 7). In the case of Pd NWs, hydrogen and oxygen diffuse to the surface of Pd NWs, and they react with Pd NWs. However, oxygen can react with adsorbed hydrogen, and adsorbed oxygen can block the active site of Pd NWs,[16,17] leading to the rapid decrease in sensing properties, including the response, recovery, and detection limit of Pd NWs (Figure 7a). On the other hand, the ZIF-8 membrane can reduce the adsorption of oxygen molecules on Pd NWs (Figure 7b). Because the gas molecules permeate through the micropores (0.34 nm) of ZIF-8, hydrogen with a kinetic dimater of 0.289 nm has high permeability in the ZIF-8 membrane, whereas the permeability of large sized molecules is extremely low.[30] Therefore, the ZIF-8 membrane on Pd NWs can effectively minimize the reaction of oxygen molecules (a kinetic diamter of 0.345 nm) on Pd. Due to these effects, Pd NWs@ZIF-8 dramatically improves the hydrogen sensing properties in terms of detection limit, response time, and recovery time. Figure 7c shows the schematic illustration of Pd NWs, Pd NWs@ZIF-8_2 h, Pd NWs@ZIF-8_4 h, and Pd NWs@ZIF-8_6 h. In the absence of a protection layer, the surface of Pd NWs exposed to air are negatively affected by oxygen molecules. In the case of Pd NWs@ZIF-8_2 h, the Pd NW is covered by ZIF-8, but there are necking points in the Pd NWs@ZIF-8, which is observed in SEM analysis (Figure 2e). When the necking points are exposed to oxygen, the adsorbed oxygen on the necking points can block the reaction sites of the Pd NW. In addition, impurities, such as hydroxide, can be slightly formed on the surface of Pd NW during the solution-based assembly process of ZIF-8 and further contribute to a dampening in H_2 response. Moreover, as the growth of ZIF-8 on Pd NWs can reduce the active sites of the Pd NWs, the response of Pd NWs@ZIF-8_2 h is decreased compared to that of the pristine Pd NWs. On the other hand, in the case of Pd NWs@ZIF-8_4 h, the Pd NW is fully covered by the ZIF-8 layers (Figure 2h) that minimize the negative effect of oxygen on Pd-based hydrogen sensors. As a result, the response of Pd NWs@ZIF-8_4 h is higher than that of Pd NWs@ZIF-8_2 h. However, Pd NWs@ZIF-8_4 h shows still a low response compared to the pristine Pd NWs because of the decrease in the reaction sites of Pd NWs caused by the growth of ZIF-8. After the assembly of ZIF-8 for 6 h, the thick layer of ZIF-8 is deposited on the surface, and the Pd NWs are embedded in the ZIF-8 layers (Figure 2k). Because the amounts of hydrogen diffused to the surface of Pd NWs are decreased compared to that with Pd NWs@ZIF-8_4 h, the response of Pd NWs@ZIF-8_6 h is decreased. However, in terms of response and

DOI: 10.1021/acsnano.7b04529
ACS Nano 2017, 11, 9276−9285

Table 1. Sensing Properties for Pd-Based Hydrogen Sensors Operated at Room Temperature in Air

materials[a]	response at 0.1% [H_2]	τ_{resp}/τ_{rec}[b] at 0.1% [H_2]	detection limit ([H_2])	ref
Pd/Ni film (t = 50 nm)	nr	120 s/20 s	nr	13
Pd NW (d = 50−80 nm)	∼1%	nr	1000 ppm	6
single Pd NW (25 (h) × 85 nm (w))	3%	400 s/1000 s	100 ppm	7
single Pd@Pt NW (40 (h) × 100 nm (w))	nr	250 s/15 s	0.2%	17
Pd nanotube	2%	80 s/nr	500 ppm	9
Pd nanotube	1000%	190 s/nr	100 ppm	10
Pd NWs@ZIF-8_2 h	0.3%	13 s/6 s	1000 ppm	this work
Pd NWs@ZIF-8_4 h	0.7%	30 s/8 s	600 ppm	this work

[a]Abbreviations: t = thickness, d = diameter, h and w are the lateral dimensions of a NW with a rectangular cross section; nr = not reported. [b]τ_{resp} is the time necessary for the resistance to increase from R_0 to the $0.9\Delta R_{max}$, and τ_{rec} is the time for the resistance to decrease from ΔR_{max} to $0.1R_0$.

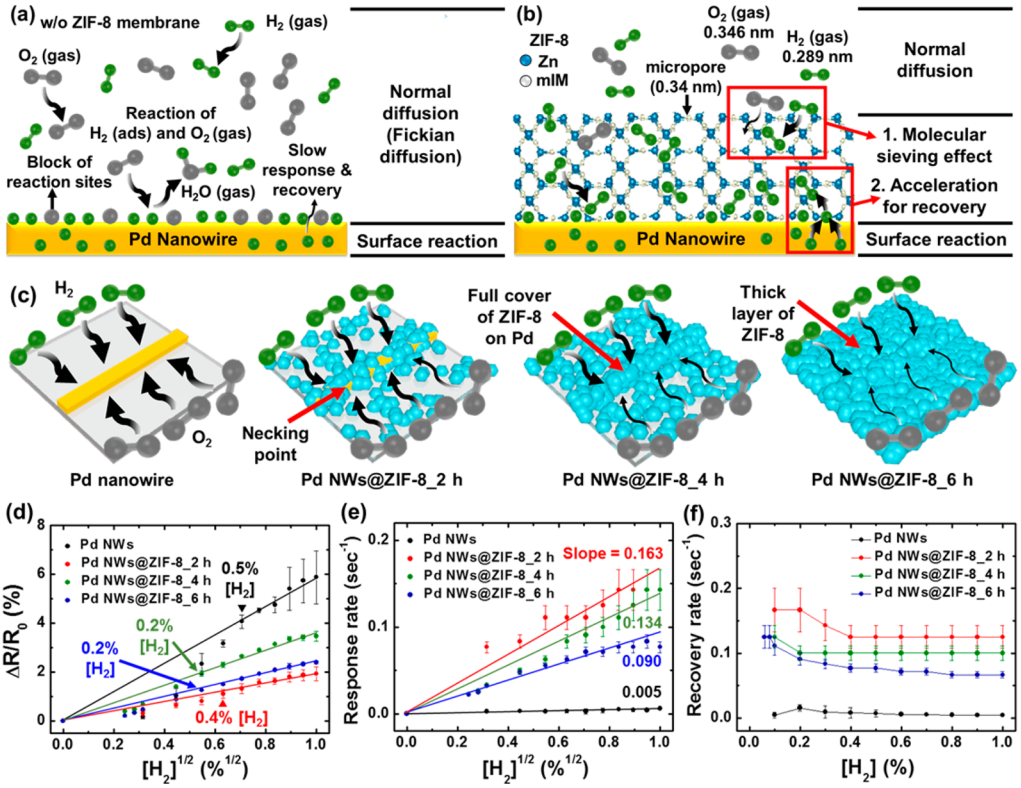

Figure 7. Schematic illustration of accelerated hydrogen sensing properties of Pd NWs@ZIF-8. (a) Sensing model for Pd NWs without ZIF-8 membrane and (b) sensing model for Pd NWs@ZIF-8. Pd NWs without ZIF-8 can be largely affected by oxygen in air. However, the micropores (0.34 nm) of ZIF-8 can act as a molecule sieving layer. Hydrogen (kinetic diameter of 0.298 nm) easily diffuses through the cavity of ZIF-8, whereas oxygen (kinetic diameter of 0.346 nm) diffusion in ZIF-8 is retarded. The hydrogen that diffuses to the surface of Pd NWs can react with Pd. In addition, ZIF-8 can improve the recovery of the sensors by the acceleration effect. (c) Schematic illustrate of the Pd NW, Pd NWs@ZIF-8_2 h, Pd NWs@ZIF-8_4 h, and Pd NWs@ZIF-8_6 h. (d) Response *versus* [$H_2^{1/2}$] in air, (e) response rate *versus* [$H_2^{1/2}$] in air, and (f) recovery rate *versus* [H_2].

recovery, the sensors exhibited clear tendency: (i) ZIF-8 decreases the response and recovery time of Pd NWs because ZIF-8 plays a role of the molecular sieving and acceleration layer. (ii) The thick ZIF-8 layer increases the response and recovery time because the diffusion length of hydrogen in ZIF-8 layer is increased.

To further demonstrate the improvement of sensors, we linearly plotted the response and response rate of the sensors *versus* $[H_2]^{1/2}$. Response rate is defined as a reciprocal of response time. Because the detection of hydrogen below 1% is explained by hydrogen diffusion into interstitial sites of Pd metals (α-PdH_x),[39] the relation between hydrogen concentration (below 1%) and response of Pd NWs can be described by Sieverts' Law.[8] The reaction of hydrogen on Pd NWs and the equilibrium constant (K) of the reaction can be written as the following equations (reaction 3 and eq 4).

$$0.5H_2\ (\text{gas}) \rightarrow H\ (\text{ads}) \tag{3}$$

$$K = (\sqrt{P_{H_2}})/(x_s) \tag{4}$$

For small values of x_s ($x < 0.015$), we can assume that $x_s \approx x$. In addition, the electrical resistivity of α-PdH_x is directly proportional to adsorbed hydrogen (x_s). Therefore, the resistance change of Pd NWs is linearly proportional to $[H_2]^{1/2}$ ($\Delta R/R_0 \propto [H_2]^{1/2}$). Because the response to 0% of [H_2] should be 0, we plotted the sensing data with the assumption that the intercept of the y-axis is 0 (Figure 7d). Basically, it will exhibit a linear relationship. However, oxygen

DOI: 10.1021/acsnano.7b04529
ACS Nano 2017, 11, 9276−9285

in air and the ZIF-8 layer on Pd NWs can influence the reaction of Pd, leading to a nonideal behavior. In the case of pristine Pd NWs, we observed an ideal relationship up to 0.5% of hydrogen. However, after that, the sensor shows a nonideal behavior, which can be explained by the Pd NWs being largely influenced by oxygen in low levels of hydrogen. On the other hand, when the ZIF-8 layer is covered on Pd NWs, the ideal behavior of the sensors is shown to be 0.4% [H_2] for Pd NWs@ZIF-8_2 h and 0.2% [H_2] for Pd NWs@ZIF-8_4 h and Pd NWs@ZIF-8_6 h. In addition, the detection limit of sensors is down to 0.06% for Pd NWs@ZIF-8_4 h and Pd NWs@ZIF-8_6 h, compared to that (0.1%) of Pd NWs. These results demonstrate that ZIF-8 membrane minimizes the oxygen effect on Pd NWs by the molecular sieving effect.

In addition, the response rate of sensors was calculated and plotted *versus* $[H_2]^{1/2}$ (Figure 7e) to investigate the difference in the response rate with and without the ZIF-8 layer. Previously, Yang *et al.*[8] demonstrated the linear relationship between response rate of Pd NWs and $[H_2]^{1/2}$ in the concentration below 1% of hydrogen. When we calculated the slope of each plotting line, we obtained values for Pd NWs@ZIF-8 higher than those for Pd NWs. In particular, the slope of Pd NWs@ZIF-8_2 h is 32.6-fold higher than that of pristine Pd NWs. Because the slope directly represents the response speed of the sensors, we confirmed that the ZIF-8 layer improves the response speed of Pd NWs, whereas an increase of the thickness of the ZIF-8 layer retards the response. Furthermore, the recovery rate of sensors is shown in Figure 7f. Recovery rate of sensors is defined as a reciprocal of response time. Similar to the response rate, we can see a noticeable improvement in the recovery rate of Pd NWs@ZIF-8, compared to that of Pd NWs. In addition, the recovery rate of Pd NWs@ZIF-8 is increased at low levels (below 0.4%) of hydrogen compared to high levels (above 0.4%) of hydrogen. It was previously reported that the introduction of MOFs on Pd crystals can increase the adsorption and desorption rate of hydrogen in Pd by enhancing the surface/bulk reactivity of the nanocrystals.[40] Therefore, the ZIF-8 near the surface of Pd NWs may accelerate the desorption of hydrogen on the Pd NWs, and the recovery rate of Pd NWs@ZIF-8 is faster at low concentrations compared to high concentrations due to the small amounts of adsorbed hydrogen in Pd. Although it is not readily explained by this mechanism, these results apparently show that the presence of the ZIF-8 layer on Pd dramatically enhances the recovery and response rates of the Pd NWs by the molecular sieving effect and the acceleration effect of ZIF-8.

CONCLUSIONS

In this work, we describe an efficient architecture for H_2 sensors in which a nanofilter is interposed between the sensing element—an array of Pd NWs in this case—and the gaseous ambient. The nanofilter, which is highly permeable to H_2 but impermeable to other large gases, is a ZIF-8 MOF layer that is synthesized directly on top of the Pd NWs from methanolic solution. Three thicknesses for this MOF layer were evaluated—a parameter controlled using the deposition time.

In terms of H_2 sensing performance, these "Pd NWs@ZIF-8 sensors" differed from pristine (unfiltered) Pd NW sensors in two ways: First, response and recovery times were more rapid by a factor of 20 or more, accelerating from a 164 s response at bare Pd NWs to just 7 s at Pd NWs@ZIF-8 sensors for the same 1% H_2 exposure. An even stronger acceleration of recovery was observed. Second, the response of the sensor to H_2 was improved modestly from 1000 ppm for pristine Pd NWs to 600 ppm for Pd NWs@ZIF-8 sensors. This performance was achieved using the thinnest ZIF-8 layers examined here, with thicknesses of 100−170 nm. Based upon previous work, the acceleration of response and recovery and the slight improvement in sensitivity are attributed to the exclusion of O_2 from the surfaces of the Pd NW sensors.

Adequate response and recovery speed are among the most important attributes for H_2 safety sensors, and they have been the most difficult to achieve in practical H_2 sensor designs—even among the many recently published examples where nanoscopic sensing elements have been employed. We demonstrate here that the imposition of a simple MOF-based nanofilter in front of the sensing element produces a dramatic acceleration of Pd NW sensors without reducing sensitivity. It is likely that this same strategy can be applied to accelerate other Pd-based sensor elements.

EXPERIMENTAL SECTION

Materials. 2-Methylimidazole (mIM, 99.0%) was purchased from Aldrich. Zinc nitrate hexahydrate ([$Zn(NO_3)_2{\cdot}6H_2O$], 98%), palladium chloride ($PdCl_2$, 99.999%), ethylenediaminetetraacetic acid (EDTA, 99.995%), and potassium chloride (KCl, 99.3%) were used as received from Sigma-Aldrich. Positive photoresist solution (Shipley S1808) and developer solution (Shipley MF-319) were purchased from Microchem. Glass substrates, acetone, methanol, and nitric acid were used as received from Fisher. Nickel (Ni) and gold (Au) targets (99.999%) were purchased from Kurt J. Lesker.

Synthesis of Pd NWs. Pd NWs with widths of 200 nm and heights of 40 nm were fabricated by LPNE process. These Pd NWs were lithographically patterned at a 10 μm pitch on the glass surface. The LPNE process used here was as follows: First, a Ni film with a thickness of 40 nm was deposited on glass substrates using a thermal evaporator. A positive photoresist (Shipley S1808) was spin-coated on the Ni/glass substrate at 2500 rpm for 80 s, and the substrate was then soft-baked at 90 °C for 30 min. Then, the photoresist layer was photopatterned using a photolithographic contact mask and UV light exposure (Newport model 97436, i-line, 365 nm, 500 W, and 2.5 s). This substrate was then immersed in the developer solution (Shipley MF-319) for 20 s, washed with deionized water, and dried in air. To produce a horizontal undercut between the photoresist and the glass substrate, the samples were etched by 0.8 M nitric acid for 5 min. The Pd NWs were synthesized by electrodeposition using a potentiostat (Gamry Instrument, G300). The lithographically patterned glass substrate was immersed in aqueous plating solution containing 0.2 mM $PdCl_2$, 0.22 mM EDTA, and 0.1 M KCl (adjusted to pH 4.9). An edge of the nickel film was electrically contacted and functioned as the working electrode. The counter electrode was a platinum foil, and the reference electrode was a saturated calomel electrode (SCE). The Pd NWs were electrodeposited at negative 0.80 V *vs* SCE. After electrodeposition, the substrate was rinsed with acetone to remove the photoresist layer. Then, the Ni layer was removed by etching in 0.8 M nitric acid.

Synthesis of Pd NWs@ZIF-8. A Pd NW patterned glass substrate was placed at the bottom of the beaker. Then, 0.293 g of $Zn(NO_3)_2{\cdot}6H_2O$ (0.293 g) and 0.649 g of mIM as precursor materials for the growth of ZIF-8 were dissolved in 30 mL of MeOH. Next, the solution was gently poured in the beaker. The coating thickness of ZIF-8 grown on Pd NWs was controlled by changing assembly time (2, 4, and 6 h) of ZIF-8 at RT. After the assembly process, the substrate was washed with the ethanol five times and dried overnight at RT.

Characterization. SEM (Magellan 400 XHR system, FEI) analysis was conducted to analyze the microstructures and morphologies of samples. EDS images were obtained using same SEM equipment with an EDS detector (80 mm^2, Aztec software, Oxford Instruments). Atomic force microscopy (MFP-3D, Asylum Research) analysis was carried out to investigate the surface morphology of pristine Pd NWs and ZIF-8-coated Pd NWs. Grazing incidence XRD (Ultima III,

DOI: 10.1021/acsnano.7b04529
ACS Nano 2017, 11, 9276−9285

Rigaku) analysis with Cu Kα radiation (λ = 1.5418 Å) was conducted to investigate the crystal structure.

Sensor Fabrication and Gas Sensing Measurement. The hydrogen sensors were prepared by evaporating Au electrodes of 60 nm thickness between NWs. The parallel Au electrodes were patterned between the Pd NWs (20 μm) and patterned glass substrate. Then, the ZIF-8 layers were introduced on the sensors using an assembly process. The resistance of samples was measured using a four-probe system with a source meter (model 2400, Keithley Instruments) and a digital multimeter (model 2000, Keithley Instruments). The sensor was placed in a sealed chamber. Pulses of a hydrogen−air mixture (0.02 to 1% H_2) were prepared by premixing H_2 with dry air, using two mass flow controllers (model 1479A, MKS Inc.) under the control of a Labview (BNC 2110, National Instruments) program. All hydrogen sensing measurements were conducted at ambient temperature (RT, ∼20 °C).

ASSOCIATED CONTENT

Supporting Information

The Supporting Information is available free of charge on the ACS Publications website at DOI: 10.1021/acsnano.7b04529.

SEM and EDS mapping images and XRD data (PDF)

AUTHOR INFORMATION

Corresponding Authors

*E-mail: idkim@kaist.ac.kr.

*E-mail: rmpenner@uci.edu.

ORCID

Il-Doo Kim: 0000-0002-9970-2218

Reginald M. Penner: 0000-0003-2831-3028

Notes

The authors declare no competing financial interest.

ACKNOWLEDGMENTS

This work was supported by the National Research Foundation (NRF) of Korea grant funded by the Ministry of Science, ICT and Future Planning (NRF-2015R1A2A1A16074901). This work was also supported by Wearable Platform Materials Technology Center (WMC) funded by National Research Foundation of Korea (NRF) Grant of the Korean Government (MSIP) (No. 2016R1A5A1009926). R.M.P. gratefully acknowledges the financial support of this work by the National Science Foundation, Chemistry Division, through Contract CHE-1306928.

REFERENCES

(1) Jacobson, M.; Colella, W.; Golden, D. Cleaning the Air and Improving Health with Hydrogen Fuel-Cell Vehicles. *Science* **2005**, *308*, 1901−1905.

(2) Russo, P. A.; Donato, N.; Leonardi, S. G.; Baek, S.; Conte, D. E.; Neri, G.; Pinna, N. Room-Temperature Hydrogen Sensing with Heteronanostructures Based on Reduced Graphene Oxide and Tin Oxide. *Angew. Chem., Int. Ed.* **2012**, *51*, 11053−11057.

(3) Potyrailo, R. A. Multivariable Sensors for Ubiquitous Monitoring of Gases in the Era of Internet of Things and Industrial Internet. *Chem. Rev.* **2016**, *116*, 11877−11923.

(4) Kim, Y. H.; Kim, S. J.; Kim, Y.-J.; Shim, Y.-S.; Kim, S. Y.; Hong, B. H.; Jang, H. W. Self-Activated Transparent All-Graphene Gas Sensor with Endurance to Humidity and Mechanical Bending. *ACS Nano* **2015**, *9*, 10453−10460.

(5) Favier, F.; Walter, E. C.; Zach, M. P.; Benter, T.; Penner, R. M. Hydrogen Sensors and Switches from Electrodeposited Palladium Mesowire Arrays. *Science* **2001**, *293*, 2227−2231.

(6) Offermans, P.; Tong, H.; Van Rijn, C.; Merken, P.; Brongersma, S.; Crego-Calama, M. Ultralow-Power Hydrogen Sensing with Single Palladium Nanowires. *Appl. Phys. Lett.* **2009**, *94*, 223110.

(7) Yang, F.; Taggart, D. K.; Penner, R. M. Fast, Sensitive Hydrogen Gas Detection using Single Palladium Nanowires that Resist Fracture. *Nano Lett.* **2009**, *9*, 2177−2182.

(8) Yang, F.; Kung, S.-C.; Cheng, M.; Hemminger, J. C.; Penner, R. M. Smaller is Faster and More Sensitive: the Effect of Wire Size on the Detection of Hydrogen by Single Palladium Nanowires. *ACS Nano* **2010**, *4*, 5233−5244.

(9) Yu, S.; Welp, U.; Hua, L. Z.; Rydh, A.; Kwok, W. K.; Wang, H. H. Fabrication of Palladium Nanotubes and Their Application in Hydrogen Sensing. *Chem. Mater.* **2005**, *17*, 3445−3450.

(10) Lim, M. A.; Kim, D. H.; Park, C.-O.; Lee, Y. W.; Han, S. W.; Li, Z.; Williams, R. S.; Park, I. A New Route toward Ultrasensitive, Flexible Chemical Sensors: Metal Nanotubes by Wet-Chemical Synthesis along Sacrificial Nanowire Templates. *ACS Nano* **2012**, *6*, 598−608.

(11) Xu, T.; Zach, M.; Xiao, Z.; Rosenmann, D.; Welp, U.; Kwok, W.; Crabtree, G. Self-Assembled Monolayer-Enhanced Hydrogen Sensing with Ultrathin Palladium Films. *Appl. Phys. Lett.* **2005**, *86*, 203104.

(12) Kaltenpoth, G.; Schnabel, P.; Menke, E.; Walter, E.; Grunze, M.; Penner, R. M. Multimode Detection of Hydrogen Gas using Palladium-Covered Silicon μ-Channels. *Anal. Chem.* **2003**, *75*, 4756−4765.

(13) Hughes, R.; Schubert, W. Thin Films of Pd/Ni Alloys for Detection of High Hydrogen Concentrations. *J. Appl. Phys.* **1992**, *71*, 542−544.

(14) Zeng, X.-Q.; Wang, Y.-L.; Deng, H.; Latimer, M. L.; Xiao, Z.-L.; Pearson, J.; Xu, T.; Wang, H.-H.; Welp, U.; Crabtree, G. W.; et al. Networks of Ultrasmall Pd/Cr Nanowires as High Performance Hydrogen Sensors. *ACS Nano* **2011**, *5*, 7443−7452.

(15) Flanagan, T. B.; Oates, W. The Palladium-Hydrogen System. *Annu. Rev. Mater. Sci.* **1991**, *21*, 269−304.

(16) Nyberg, C.; Tengstål, C. Adsorption and Reaction of Water, Oxygen, and Hydrogen on Pd (100): Identification of Adsorbed Hydroxyl and Implications for the Catalytic H_2−O_2 Reaction. *J. Chem. Phys.* **1984**, *80*, 3463−3468.

(17) Li, X.; Liu, Y.; Hemminger, J. C.; Penner, R. M. Catalytically Activated Palladium@ Platinum Nanowires for Accelerated Hydrogen Gas Detection. *ACS Nano* **2015**, *9*, 3215−3225.

(18) Lee, J.; Farha, O. K.; Roberts, J.; Scheidt, K. A.; Nguyen, S. T.; Hupp, J. T. Metal−Organic Framework Materials as Catalysts. *Chem. Soc. Rev.* **2009**, *38*, 1450−1459.

(19) Li, J.-R.; Kuppler, R. J.; Zhou, H.-C. Selective Gas Adsorption and Separation in Metal−Organic Frameworks. *Chem. Soc. Rev.* **2009**, *38*, 1477−1504.

(20) Lu, G.; Hupp, J. T. Metal−Organic Frameworks as Sensors: a ZIF-8 based Fabry− Pérot Device as a Selective Sensor for Chemical Vapors and Gases. *J. Am. Chem. Soc.* **2010**, *132*, 7832−7833.

(21) Koo, W.-T.; Choi, S.-J.; Kim, S.-J.; Jang, J.-S.; Tuller, H. L.; Kim, I.-D. Heterogeneous Sensitization of Metal−Organic Framework Driven Metal@ Metal Oxide Complex Catalysts on an Oxide Nanofiber Scaffold Toward Superior Gas Sensors. *J. Am. Chem. Soc.* **2016**, *138*, 13431−13437.

(22) Kreno, L. E.; Leong, K.; Farha, O. K.; Allendorf, M.; Van Duyne, R. P.; Hupp, J. T. Metal−Organic Framework Materials as Chemical Sensors. *Chem. Rev.* **2012**, *112*, 1105−1125.

(23) Horcajada, P.; Chalati, T.; Serre, C.; Gillet, B.; Sebrie, C.; Baati, T.; Eubank, J. F.; Heurtaux, D.; Clayette, P.; Kreuz, C.; et al. Porous Metal-Organic-Framework Nanoscale Carriers as a Potential Platform for Drug Delivery and Imaging. *Nat. Mater.* **2010**, *9*, 172−178.

(24) Eddaoudi, M.; Kim, J.; Rosi, N.; Vodak, D.; Wachter, J.; O'keeffe, M.; Yaghi, O. M. Systematic Design of Pore Size and Functionality in Isoreticular MOFs and Their Application in Methane Storage. *Science* **2002**, *295*, 469−472.

(25) Xia, W.; Mahmood, A.; Zou, R.; Xu, Q. Metal−Organic Frameworks and Their Derived Nanostructures for Electrochemical

DOI: 10.1021/acsnano.7b04529
ACS Nano 2017, 11, 9276−9285

Energy Storage and Conversion. *Energy Environ. Sci.* **2015**, *8*, 1837−1866.
(26) Zhou, H.-C.; Kitagawa, S. Metal−organic frameworks (MOFs). *Chem. Soc. Rev.* **2014**, *43*, 5415−5418.
(27) Furukawa, H.; Cordova, K. E.; O'Keeffe, M.; Yaghi, O. M. The Chemistry and Applications of Metal-Organic Frameworks. *Science* **2013**, *341*, 1230444.
(28) Park, K. S.; Ni, Z.; Côté, A. P.; Choi, J. Y.; Huang, R.; Uribe-Romo, F. J.; Chae, H. K.; O'Keeffe, M.; Yaghi, O. M. Exceptional Chemical and Thermal Stability of Zeolitic Imidazolate Frameworks. *Proc. Natl. Acad. Sci. U. S. A.* **2006**, *103*, 10186−10191.
(29) Cravillon, J.; Münzer, S.; Lohmeier, S.-J.; Feldhoff, A.; Huber, K.; Wiebcke, M. Rapid Room-Temperature Synthesis and Characterization of Nanocrystals of a Prototypical Zeolitic Imidazolate Framework. *Chem. Mater.* **2009**, *21*, 1410−1412.
(30) Huang, A.; Liu, Q.; Wang, N.; Zhu, Y.; Caro, J. Bicontinuous Zeolitic Imidazolate Framework ZIF-8@GO Membrane with Enhanced Hydrogen Selectivity. *J. Am. Chem. Soc.* **2014**, *136*, 14686−14689.
(31) Pan, Y.; Wang, B.; Lai, Z. Synthesis of Ceramic Hollow Fiber Supported Zeolitic Imidazolate Framework-8 (ZIF-8) Membranes with High Hydrogen Permeability. *J. Membr. Sci.* **2012**, *421-422*, 292−298.
(32) Drobek, M.; Kim, J.-H.; Bechelany, M.; Vallicari, C.; Julbe, A.; Kim, S. S. MOF-Based Membrane Encapsulated ZnO Nanowires for Enhanced Gas Sensor Selectivity. *ACS Appl. Mater. Interfaces* **2016**, *8*, 8323−8328.
(33) Wu, X.; Xiong, S.; Mao, Z.; Hu, S.; Long, X. A Designed ZnO@ZIF-8 Core-Shell Nanorods Film as Gas Sensor with Excellent Selectivity of H_2 over CO. *Chem. - Eur. J.* **2017**, *23*, 7969−7975.
(34) Kim, I.-D.; Rothschild, A.; Tuller, H. L. Advances and New Directions in Gas-Sensing Devices. *Acta Mater.* **2013**, *61*, 974−1000.
(35) *Funding Opportunity Announcement DE-PS36-09GO99004*, Office of Energy Efficiency and Renewable Energy (EERE), 2009.
(36) Thanh, N. T.; Maclean, N.; Mahiddine, S. Mechanisms of Nucleation and Growth of Nanoparticles in Solution. *Chem. Rev.* **2014**, *114*, 7610−7630.
(37) Koo, W.-T.; Jang, J.-S.; Choi, S.-J.; Cho, H.-J.; Kim, I.-D. Metal-Organic Framework Templated Catalysts: Dual Sensitization of PdO-ZnO Composite on Hollow SnO_2 Nanotubes for Selective Acetone Sensors. *ACS Appl. Mater. Interfaces* **2017**, *9*, 18069−18077.
(38) Usman, M.; Mendiratta, S.; Lu, K.-L. Semiconductor Metal-Organic Frameworks: Future Low-Bandgap Materials. *Adv. Mater.* **2017**, *29*, 1605071.
(39) Lewis, F. A. *The Palladium Hydrogen System*; Academic Press: London, 1967.
(40) Li, G.; Kobayashi, H.; Taylor, J. M.; Ikeda, R.; Kubota, Y.; Kato, K.; Takata, M.; Yamamoto, T.; Toh, S.; Matsumura, S.; et al. Hydrogen Storage in Pd Nanocrystals Covered with a Metal−Organic Framework. *Nat. Mater.* **2014**, *13*, 802−806.

DOI: 10.1021/acsnano.7b04529
ACS Nano 2017, 11, 9276−9285